Photoionization-induced dynamics of ammonia: Ab initio potential energy surfaces and time-dependent wave packet calculations for the ammonia cation

Alexandra Viel, Wolfgang Eisfeld, Stefanie Neumann, Wolfgang Domcke, Uwe Manthe

Photoionization-induced dynamics of ammonia: *Ab initio* potential energy surfaces and time-dependent wave packet calculations for the ammonia cation

Alexandra Viel[a)]
Laboratoire de Physique des Atomes, Lasers, Molécules et Surfaces (PALMS), CNRS UMR 6627, Université de Rennes 1, Campus de Beaulieu, F-35042 Rennes, France

Wolfgang Eisfeld,[b)] Stefanie Neumann, and Wolfgang Domcke
Theoretische Chemie, Department Chemie, Technische Universität München, D-85747 Garching, Germany

Uwe Manthe
Theoretische Chemie, Fakultät für Chemie, Universität Bielefeld, Postfach 100131, D-33501 Bielefeld, Germany

(Received 9 March 2006; accepted 12 April 2006; published online 5 June 2006)

An analytical anharmonic six-dimensional three-sheeted potential energy surface for the ground and first excited states of the ammonia cation has been developed which is tailored to model the ultrafast photoinduced dynamics. Selected *ab initio* cuts, obtained by multireference configuration interaction calculations, have been used to determine the parameters of a diabatic representation for this Jahn-Teller and pseudo-Jahn-Teller system. The model includes higher-order coupling terms both for the Jahn-Teller and for the pseudo-Jahn-Teller matrix elements. The relaxation to the ground state is possible via dynamical pseudo-Jahn-Teller couplings involving the asymmetric bending and stretching coordinates. The photoelectron spectrum of NH_3 and the internal conversion dynamics of NH_3^+ have been determined by wave packet propagation calculations employing the multiconfigurational time-dependent Hartree method. Three different time scales are found in the dynamics calculations for the second absorption band. The ultrafast Jahn-Teller dynamics of the two excited states occurs on a 5 fs time scale. The major part of the internal conversion to the ground state takes place within a short time scale of 20 fs. This fast internal conversion is, however, incomplete and the remaining excited state population does not decay completely even within 100 fs. © *2006 American Institute of Physics*. [DOI: 10.1063/1.2202316]

I. INTRODUCTION

The photoelectron spectrum of ammonia and the associated dynamics of NH_3^+ have been a topic of interest for decades. The outer-valence photoelectron spectrum consists of two bands, corresponding to ionization from the $3a_1$ and $1e$ orbitals of NH_3. These orbitals are the bonding linear combinations of the $2p_z$ and $2p_{x,y}$ orbitals of nitrogen, respectively, with the $1s$ orbitals of the hydrogen atoms. Photoelectron spectra of ammonia have been obtained with He I and He II UV radiations, x-ray radiation, as well as with synchrotron radiation, see, e.g., Refs. 1–4. The most recent investigation of Edvardsson *et al.* of He I and He II photoelectron spectra of ammonia provides a comprehensive list of references.[5]

The band corresponding to the electronic ground state of NH_3^+, resulting from the ionization out of the $3a_1$ orbital, exhibits an extended progression in the symmetric bending (umbrella) vibration ν_2. The strong excitation of the umbrella vibration is the consequence of the transition from a pyramidal to a planar equilibrium geometry upon ionization, in accordance with Walsh's rules.[1] The assignment of the origin of the main ν_2 progression as well as the origin of a second, much less intense, ν_2 progression has been discussed controversially in the literature.[5–7] According to the most recent assignment, the intensity maximum of the ν_2 progression occurs at $\nu_2=6$ and the secondary ν_2 progression is built on a single quantum of the asymmetric bending mode ν_4.[5]

The band corresponding to the first excited electronic state of NH_3^+, resulting from the ionization of the $1e$ orbital, is very broad. In contrast to the $\tilde{X}\,^2A_1$ band, it exhibits only weak, diffuse, and irregular vibronic structures.[1–5] It was shown by Haller *et al.* that the vibronic structure of this band is dominated by a two-mode Jahn-Teller (JT) effect, involving strong JT coupling of the asymmetric bending as well as stretching modes.[8] An interesting aspect of the first excited state is the absence of detectable radiative emission, even for levels which are below the lowest dissociation limit of NH_3^+.[9] It has been conjectured that a conical intersection between the excited and the ground state potential energy (PE) surfaces may lead to ultrafast internal conversion which quenches the fluorescence.[9,10]

In 2003, the nonadiabatic coupling of the ground and excited states of NH_3^+ has been studied for the first time via time-dependent quantum wave packet calculations within a linear vibronic coupling model in the C_{3v} symmetry group.[11]

[a)]Electronic mail: alexandra.viel@univ-rennes1.fr
[b)]Electronic mail: wolfgang.eisfeld@ch.tum.de

In the C_{3v} point group, the $^2A_1$ ground and ^2E excited electronic states can interact via degenerate vibrational modes of e symmetry. This phenomenon is known as the pseudo-JT (PJT) effect.[12–15] The model was based on a diabatic representation[16–18] of the electronic states. The diagonal and off-diagonal elements of the 3×3 PE matrix have been expressed as low-order Taylor expansions in terms of the normal coordinates.[15,19,20] According to the model of Woywod *et al.*,[11] the pronounced JT splitting of the $\tilde{A}\,^2E$ state together with the $\tilde{X}\,^2A_1$-$\tilde{A}\,^2E$ PJT coupling result in a conical intersection[21,22] of the $\tilde{X}$ and $\tilde{A}$ PE surfaces.

However, this first study contains several points which call for improvement. First of all, the coordinate system used is not suitable to represent the large-amplitude motion of the umbrella mode. Second, analysis of the involved electronic states in D_{3h} symmetry reveals that the PJT coupling has to vanish for planar geometries. The PJT coupling constant thus must exhibit a significant dependence on the umbrella angle. Since the equilibrium geometry of the ionic ground state is planar, this must be taken into account in the theoretical model. Third, the preparation of the excited state of NH_3^+ by vertical photoionization results in large-amplitude motions in the three bending degrees of freedom. In addition, the asymmetric stretching vibration exhibits significant JT activity. The vibronic coupling model employed in Ref. 11, being based on low-order Taylor expansions in normal coordinates, therefore must have its limitations, in particular, for the bending modes. A more complete and more accurate description of the photoionization-induced dynamics of NH_3^+ should be based on global anharmonic six-dimensional (6D) PE surfaces of the ground and excited states, with inclusion of the pronounced non-Born-Oppenheimer effects caused by the JT and dynamical PJT couplings.

Six-dimensional PE surfaces of the ground state of NH_3^+ have been constructed by Léonard *et al.*,[23–25] however, without inclusion of nonadiabatic couplings with the excited state. An anharmonic (up to quartic terms) force field has been obtained by density functional theory (DFT), employing the B97-1 functional, and by coupled-cluster methods [restricted CCSD(T)].[23] A full six-dimensional analytic representation of the PE function of the ground state in internal coordinates has been constructed based on restricted CCSD(T) calculations.[24] Agreement to within 2 cm^{-1} between calculated vibrational energy levels and experimental data has been obtained for low vibrational levels of several isotopes.[24] Similar studies of the ground state potential energy surface of neutral NH_3 and the resulting vibrational energy levels were published by the groups of Halonen[26,27] and Thiel.[28]

The long-term goal must be the construction of global coupled PE surfaces of the ground and excited states of NH_3^+ at a similar level of accuracy. The presence of conical intersections renders the construction of a diabatic representation indispensable, both for an efficient interpolation of the adiabatic PE surfaces as well as for an efficient treatment of the nuclear dynamics in the vicinity of the conical intersections.[22,29] The difficulties associated with the accurate calculation of excited electronic states and the construction of a diabatic representation of multiply intersecting surfaces constitute a considerable challenge. Two of the authors have recently proposed a systematic derivation of the diabatic representation of such a Jahn-Teller and pseudo-Jahn-Teller system (with a C_3 symmetry axis).[30,31] The resulting 3×3 diabatic potential matrix contains higher order terms which allow to take into account both the anharmonicity effects and the nonlinearity of the couplings between the three surfaces.

In the present work, a full-dimensional anharmonic analytical representation of the three lowest electronic states of NH_3^+ cation is presented. The photoinduced dynamics is investigated by means of time-dependent wave packet propagation on these coupled surfaces making use of the efficient multiconfiguration time-dependent Hartree (MCTDH) method for this six-dimensional problem.

II. THE NH_3^+ SYSTEM

A. Symmetry considerations

The photoionization dynamics of NH_3 is strongly influenced by the high symmetry of this system. The neutral ground state of NH_3 exhibits a C_{3v} equilibrium geometry, giving rise to a double-well potential along the umbrella vibrational mode. In contrast, the ionic ground state has a planar equilibrium geometry of D_{3h} point group symmetry and the electronic wave function transforms like $^2A_2''$. The first excited state of the ion is a degenerate ^2E state in C_{3v}, but corresponds to a $^2E'$ state in D_{3h}. This has far-reaching consequences for the vibronic coupling to the ionic ground state. Upon stepwise relaxation of geometry restrictions, one finds that the $^2E'$ state prefers a pyramidalized structure when only the restriction to planarity is lifted. Of course, the Jahn-Teller effect results in a further distortion, resulting in three equivalent minima of C_s symmetry for a fully relaxed geometry optimization.

Photoionization to the second cation state should be followed by several processes such as radiative or radiationless decay to the ground state or dissociation. Experimental results indicate that dissociation plays no significant role and no fluorescence can be observed.[9] Thus, an efficient mechanism for radiationless decay must be assumed, presumably via the pseudo-Jahn-Teller effect which couples the $^2A_1$ and ^2E states (in C_{3v} symmetry) through appropriate vibrational modes.

For systems with a C_3 symmetry axis, the PJT coupling effect has been investigated for a long time.[12,15,20] NH_3 has four vibrational modes, two which transform like a_1 (symmetric stretch and umbrella) and two which transform like e (asymmetric stretch and bend, respectively). The modes of the planar NH_3^+ transform like a_1', a_2'', e', and e'. As a result, in C_{3v} symmetry the states $^2A_1$ and ^2E of the cation are coupled by the e modes, since $A_1\otimes E\otimes e\supset A_1$. However, for the planar D_{3h} geometry, the $^2A_2''$ and $^2E'$ states are not coupled by any single mode because there does not exist an e'' mode in this molecule. It turns out that only combined motions along the e' and a_2'' modes can lead to coupling of these electronic states. The PJT coupling strength is thus tuned by the motion along the umbrella mode. For the photo-

TABLE I. Definition of the symmetry-adapted coordinates used to represent the distortions of the molecule (see text).

Coordinate	Symmetry	Definition
Symmetric stretch	a_1'	$S_1=\frac{1}{\sqrt{3}}(\Delta r_1+\Delta r_2+\Delta r_3)$
Umbrella	a_2''	$S_2=\Delta\beta$
Asymmetric stretch	e_x'	$S_3=\frac{1}{\sqrt{6}}(2\Delta r_1-\Delta r_2-\Delta r_3)$
Asymmetric stretch	e_y'	$S_4=\frac{1}{\sqrt{2}}(\Delta r_2-\Delta r_3)$
Asymmetric bend	e_x'	$S_5=\frac{1}{\sqrt{6}}(2\Delta\alpha_1-\Delta\alpha_2-\Delta\alpha_3)$
Asymmetric bend	e_y'	$S_6=\frac{1}{\sqrt{2}}(\Delta\alpha_2-\Delta\alpha_3)$

ionization dynamics of NH_3 this is a very important effect because of the planar equilibrium geometry of the ionic ground state. It is easily imagined that nonadiabatic transitions between the ground and the excited state will be inhibited when the wave packet reaches the ground state because it will tend to localize at planar geometries and thereby "switch off" the PJT coupling. For this reason, it is very important to include this effect in the theoretical treatment of the dynamics.

B. Symmetry-adapted coordinates

The PE surfaces are expanded with respect to a D_{3h} reference geometry, for which the planar equilibrium geometry of NH_3^+ has been used. Distortions from this geometry have been considered along a set of six symmetry-adapted coordinates. These correspond to the symmetric stretching coordinate of a_1' symmetry, the a_2'' symmetric bending coordinate, the doubly degenerate asymmetric stretching, and the doubly degenerate asymmetric bending coordinates of e' symmetry. Table I gives the geometric definition of the coordinates in terms of displacements in internal bond distances and angles. The umbrella coordinate S_2 is taken as the variation of the pyramidalization angle β defined as the angle between any of the NH bonds and the trisector. The definition of the trisector, going through the nitrogen atom, is such that the angles between the trisector and each of the NH bonds are identical. Planarity is therefore defined by $\beta=90°$. Since the symmetry coordinate S_2 is defined as displacement with respect to the reference geometry, a value of zero corresponds to planarity. For the definition of the asymmetric bending coordinates, the variation of the projections α_1, α_2, and α_3, of the HNH angles on a plane perpendicular to the trisector have been chosen rather than the HNH angles themselves. This ensures a correct description of large-amplitude motions. The definitions of the stretching coordinates, S_1, S_3, and S_4, are based on the variation of the NH bond lengths, r_1, r_2 and r_3, with respect to the reference geometry.

C. Potential energy matrix and vibronic coupling pattern

The description of the vibronic coupling pattern used in this study is based on the "diabatization by ansatz" approach (see Ref. 32 and Chap. 4 in Ref. 22). The diabatic potential energy matrix, including all coupling elements among the $^2A_2''$ and $^2E'$ states, is derived based on symmetry considerations. The D_{3h} point group is used, because this is the highest symmetry of the system. The usual vibronic coupling approach is extended to higher-order coupling in both the JT and the PJT coupling elements to account for the strong anharmonicity effects present in the NH_3^+ system. The uncoupled state energies also are expressed by higher-order expansions rather than using the harmonic approximation. The explicit form of the corresponding matrix elements was developed recently by two of the authors[30,31] and will not be discussed here in detail.

The 3×3 diabatic potential energy matrix $\mathbf{V}$ is expressed in symmetry-adapted coordinates $\mathbf{S}$. S_1 refers to totally symmetric stretching, S_2 corresponds to the umbrella motion, S_3 and S_4 are the components of the e' stretching, and S_5 and S_6 the components of the e' bending mode. The explicit definitions of these coordinates are summarized in Table I.

The full potential matrix is modeled considering several contributions according to the involved coordinates and coupling mechanisms as

$$\mathbf{V}=\mathbf{V}^{(0)}+\mathbf{V}^{(S_1)}+\mathbf{V}^{(S_2)}+\mathbf{V}^{\mathrm{diag}}+\mathbf{V}^{\mathrm{JT}}+\mathbf{V}^{\mathrm{PJT}}. \tag{1}$$

The constant diagonal matrix $\mathbf{V}^{(0)}$ is used to account for the vertical excitation energy between the lower and upper surfaces. The nondegenerate coordinate S_1 does not couple the electronic states directly and thus is treated separately. The potentials along the totally symmetric S_1 coordinate are given by the diagonal matrix

$$\mathbf{V}^{(S_1)}=\begin{pmatrix} V_A^{(S_1)} & 0 & 0 \\ 0 & V_E^{(S_1)} & 0 \\ 0 & 0 & V_E^{(S_1)} \end{pmatrix}, \tag{2}$$

in which the matrix elements correspond to modified Morse functions

$$\begin{aligned} V_j^{(S_1)} &= D_j^{(2)}\{1-\exp[\alpha_j(r_j-S_1)]\}^2 \\ &\quad + D_j^{(3)}\{1-\exp[\alpha_j(r_j-S_1)]\}^3 \\ &\quad - D_j^{(2)}\{1-\exp[\alpha_j r_j]\}^2 \\ &\quad - D_j^{(3)}\{1-\exp[\alpha_j r_j]\}^3 \quad (j=A,E) \end{aligned} \tag{3}$$

for the $^2A_2''$ and the $^2E'$ states. In this definition, the location of the potential minimum is determined by the free parameter r_j, which is obtained by fitting. The energies $V_j^{(S_1)}$ at the reference point $S_1=0$ are zero. The functional form of Eq. (3) allows for a simple, but accurate, treatment of the anharmonicity of this mode. The potentials along the umbrella coordinate S_2 are approximated by the power series

$$\mathbf{V}^{(S_2)}=\sum_{n=1}^{4}\frac{1}{(2n)!}\begin{pmatrix} u_A^{(n)} & 0 & 0 \\ 0 & u_E^{(n)} & 0 \\ 0 & 0 & u_E^{(n)} \end{pmatrix}S_2^{2n}. \tag{4}$$

The $^2A_2''$ and $^2E'$ states are represented by different sets of parameters, u_A and u_E. The potential functions along the JT and PJT active e' coordinates are more complicated and can be split into the diagonal potentials $\mathbf{V}^{\mathrm{diag}}$ and the coupling

matrices $\mathbf{V}^{\mathrm{JT}}$ and $\mathbf{V}^{\mathrm{PJT}}$. The diagonal matrix for the potentials along the e' coordinates reads

$$\mathbf{V}^{\mathrm{diag}} = \begin{pmatrix} V_A^{\mathrm{diag}} & 0 & 0 \\ 0 & V_E^{\mathrm{diag}} & 0 \\ 0 & 0 & V_E^{\mathrm{diag}} \end{pmatrix}. \tag{5}$$

The matrix elements are expanded in terms of the recently derived $\mathcal{V}$ functions which fulfill the symmetry conditions of a D_{3h} symmetric JT and PJT system. The explicit form of the $\mathcal{V}$ (and the $\mathcal{W}$ and $\mathcal{Z}$) expressions can be found in Refs. 30 and 31. The matrix elements V_j^{diag} are expanded in the e' bending and along the e' stretching coordinates according to

$$V_j^{\mathrm{diag}} = \sum_{k=3,5} \sum_{n=0} \frac{1}{n!} \mathcal{V}^{(n)}(S_k, S_{k+1}; \mathbf{a}^{(n)}(j,k)) \quad (j = A,E). \tag{6}$$

The parameters $\mathbf{a}^{(n)}(j,k)$ and the order of the expansions in the different modes and for both states are determined during the fitting as described in Sec. II E. The JT coupling matrix also depends on both sets of e' coordinates and reads

$$\mathbf{V}^{\mathrm{JT}} = \sum_{k=3,5} \sum_{n=1} \frac{1}{n!} \begin{pmatrix} 0 & 0 & 0 \\ 0 & \mathcal{W}^{(n)}(S_k, S_{k+1}; \lambda_{\mathrm{JT}}^{(n)}(k)) & \mathcal{Z}^{(n)}(S_k, S_{k+1}; \lambda_{\mathrm{JT}}^{(n)}(k)) \\ 0 & \mathcal{Z}^{(n)}(S_k, S_{k+1}; \lambda_{\mathrm{JT}}^{(n)}(k)) & -\mathcal{W}^{(n)}(S_k, S_{k+1}; \lambda_{\mathrm{JT}}^{(n)}(k)) \end{pmatrix}, \tag{7}$$

where the $\lambda_{JT}^{(n)}(k)$ denote the specific parameters for each pair of coordinates k and expansion order n. The PJT coupling matrix is expressed analogously, which results in

$$\mathbf{V}^{\mathrm{PJT}} = S_2 \sum_{k=3,5} \sum_{n=1} \frac{1}{n!} \begin{pmatrix} 0 & \mathcal{W}^{(n)}(S_k, S_{k+1}; \lambda_{\mathrm{PJT}}^{(n)}(k)) & -\mathcal{Z}^{(n)}(S_k, S_{k+1}; \lambda_{\mathrm{PJT}}^{(n)}(k)) \\ \mathcal{W}^{(n)}(S_k, S_{k+1}; \lambda_{\mathrm{PJT}}^{(n)}(k)) & 0 & 0 \\ -\mathcal{Z}^{(n)}(S_k, S_{k+1}; \lambda_{\mathrm{PJT}}^{(n)}(k)) & 0 & 0 \end{pmatrix}. \tag{8}$$

Note that the entire matrix is multiplied by the umbrella coordinate S_2 to account for the dependence of the PJT coupling on the umbrella angle, as discussed above. The definition of S_2 is chosen such that $S_2=0$ corresponds to the planar configuration. The explicit dependence of V^{PJT} on the S_2 coordinate also introduces an indirect coupling of the e' bending and the e' stretching modes. An explicit coupling of these sets of degenerate modes is not included in the Hamiltonian. The coupling orders in the above matrices are determined during the fitting procedure and refer to the highest orders which were considered in the fitting of the potential surfaces. The details of how the parameters of the full potential matrix are obtained will be discussed in Sec. II E.

D. *Ab initio* calculations

The PE surfaces of the $^2A_2''$ ground state and the $^2E'$ first excited state of NH_3^+ have been determined by *ab initio* calculations at the multireference configuration interaction (MRCI) level of theory. The reference wave functions were optimized by complete active space self-consistent-field (CASSCF) calculations and the reference configuration space was chosen to be of the CAS type. The active space in the CASSCF and MRCI calculations comprised the seven valence orbitals of the ammonia cation. In the CASSCF calculations, the 1*s* orbital of the nitrogen atom was optimized but excluded from the excitation pattern. This core orbital was not correlated in the MRCI calculations.

To guarantee a balanced description of several states and the stability of the wave function, six roots have been state averaged in the CASSCF wave function optimizations, although only four roots were computed in the MRCI calculations. The second excited state of A_1' symmetry has been included to account for interactions with the E_x' component of the first excited $^2E'$ state since both fall into the same symmetry when the molecule is distorted along the e' coordinates.

The vertical ionization potential (IP) to the ionic ground state was computed by coupled-cluster calculations [RCCSD(T)] because, in contrast to MRCI, RCCSD(T) is a size-extensive method. The second IP was then calculated from this first vertical IP and the vertical $\tilde{A}\,^2E' \leftarrow \tilde{X}\,^2A_2''$ excitation energy obtained by MRCI.

The basis set used for all the calculations was the augmented correlation consistent polarized valence quadruple zeta (aug-cc-pVQZ) basis set by Dunning[33] and Kendall *et al.*[34] All calculations have been performed using the MOLPRO program package.[35]

E. Fitting of the PES

The parameters in the analytic expressions of the diabatic PE matrix $\mathbf{V}$ (cf. Sec. II C) have been determined by nonlinear least-squares fitting of the eigenvalues of $\mathbf{V}$ with respect to the adiabatic state energies obtained from the *ab initio* calculations. Due to the large number of highly non-

linearly coupled parameters in **V**, which have to be optimized, it is very difficult, if not impossible, to find the global minimum of the root-mean-square (rms) error in parameter space. For this reason, we devised a genetic algorithm into which a standard Marquardt-Levenberg procedure is embedded. Nevertheless, it is important to follow a certain strategy to obtain good and reliable results. This strategy and the corresponding fitting results are discussed in the following.

The energy range of the fitted data points is about 90 000 cm^{-1} or roughly 11 eV with respect to the ionic ground state minimum. This corresponds to maximum energies of about 21 eV above the neutral ground state, which is considerably more than the energy of the wave packet considered in this work. The huge energy range to be covered together with the necessity to treat coupled surfaces poses a considerable challenge.

The diabatic energy matrix **V**, given in Sec. II C, is fitted in a step-by-step procedure. The potentials for the ground and the first excited states of NH_3^+ along the symmetric stretching coordinate S_1 are reproduced in separate fits with a rms error of about 300 cm^{-1}. For displacements along the umbrella coordinate S_2, an error of roughly 35 cm^{-1} is obtained. At first glance, a rms fitting error of 300 cm^{-1} seems rather large in comparison to other published surfaces. For example, the very accurate surface for the ammonia ground state by Lin *et al.*[28] shows a rms error of only 5 cm^{-1}. However, this surface was only fitted for energies up to 30 000 cm^{-1} and only for one electronic state, while in the present study three coupled surfaces are represented up to 90 000 cm^{-1}. The largest errors occur for high energies where the accuracy of the potentials plays a much lesser role than in the region around the potential minima where the errors are much smaller.

The two-dimensional potentials along the two sets of e' coordinates have first been fitted in separate calculations. For the representation of the e' bending potentials, it turned out to be necessary to include seventh and eighth order terms in V_A^{diag} for the ionic ground state to account for the extremely strong anharmonicity. The explicit expressions for the seventh and eighth order terms of $\mathcal{V}_A^{(n)}$ are presented in Appendix A, because they were not given in the previous publications. The V_E^{diag} elements for the excited state need only to be expanded up to sixth order to obtain the desired accuracy. For the potentials along the e' stretching coordinates, S_3 and S_4, an expansion up to sixth order was sufficient to describe the behavior of both the ground and excited state potentials.

To obtain a first estimate of the parameters of the JT matrix elements, they have been fitted for a planar geometry, considering only displacements along the pairs S_3, S_4, and S_5, S_6, respectively. Note that the components of degenerate coordinates always should be fitted together. Otherwise, deficiencies in the ansatz of the potentials will lead to distortions and a poor representation of the component which is not included explicitly. We made use of the fact that the PJT coupling vanishes for planar geometries for NH_3^+, which allows us to consider pure JT coupling along these particular cuts. To account for the PJT effect, displacements along the e' coordinates with a constant, nonzero value for the umbrella coordinate S_2 have been performed and fitted in the next step. The JT parameters, obtained from the fit for planar geometries, have initially been kept fixed and only the PJT parameters have been fitted. The procedure was continued by simultaneously fitting all the JT and PJT parameters for a complete set of displacements of the e' stretching and bending coordinates for both planar and pyramidal geometries. Finally, the JT and PJT matrix elements have been fitted to all *ab initio* data for planar and pyramidal geometries. This set of data includes combined displacements along pairs of coordinates S_3, S_4 and S_5, S_6 for which fixed ratios of $S_4 = \frac{4}{25\sqrt{3}} S_3$ and $S_6 = \frac{3}{5\sqrt{3}} S_5$ have been used.[36] This way, the accuracy of the surfaces over the full two-dimensional configurational subspaces has been improved.

To find a compromise between the number of parameters in **V** and the accuracy of the fit, the orders of the expansions have been increased successively during the fitting procedure and decisions concerning the number of parameters have been made according to the fitting error. It turned out that for the JT matrix elements, the sixth order has been necessary and sufficient for both the stretching and bending coordinates. For the PJT part, it was found that a fifth order expansion is sufficient to obtain an accurate representation of the potential cuts along the stretching coordinates since additional sixth order terms hardly reduce the error. This fitting procedure results in rms errors of about 200 cm^{-1} for the potential along the e' stretching coordinate and of approximately 550 cm^{-1} for the potential of the e' bending coordinate.

The full set of *ab initio* data, which was used for the fitting, included a total number of 385 points. Table II summarizes the distribution of the data points over the six coordinates and their combinations and also gives the range of maximum displacements for each of them. Depending on the coordinate, points with energies up to slightly different maximum values have been included in the fitting. For the fitting of the e' bending potentials, data points with energies up to 19.86 eV above the NH_3 ground state energy at the C_{3v} equilibrium geometry have been used. For the fitting of the e' stretching potentials, data points with energies up to 20.96 eV have been considered. Both values are well above the maximum energy components of the wave packet.

Figures 1–3 compare the *ab initio* data (open circles) to the adiabatic energies given by the fit (solid lines). From Fig. 1 it becomes apparent that a conical intersection is present along the S_2 coordinate, which stresses the importance of this mode. The intersection is found at an energy of roughly 17.5 eV and should have a significant influence on the observed PE spectrum and the nonadiabatic dynamics. However, the corresponding umbrella angle of 0.9 is significantly larger than the one at the minimum of the excited state potential and the equilibrium angle of the neutral ground state.

Figures 2 and 3 display the adiabatic energies obtained from the fit (solid lines) and the diabatic energies (dashed lines) along two particular cuts together with the *ab initio* data (open circles). The top panels correspond to displacements along the bending coordinate S_5, whereas the lower panels correspond to combined displacements along S_5 and S_6, imposing the constraint $S_6 = \frac{3}{5\sqrt{3}} S_5$. In Fig. 2, the molecu-

TABLE II. Number of computed data points N for the displacements along the symmetry-adapted coordinates and combinations of them. r_{max} gives the maximum range of coordinate displacements for the data points in a.u. For the combination of coordinates the displacements are given for S_3 and S_5, respectively.

Coordinate	N	r_{max}
S_1	28	−1.637 to 2.782
S_2	29	−1.222 to 1.222

	$S_2=0$		$S_2=-0.434$	
	N	r_{max}	N	r_{max}
S_3	31	−1.157 to 2.314	26	−1.157 to 1.736
S_4	21	−1.336 to 1.336	25	−1.603 to 1.603
S_3 (with $S_4=\frac{4}{25\sqrt{3}}S_3$)	21	−1.157 to 1.157	21	−1.157 to 1.157
S_5	39	−2.223 to 4.275	28	−2.052 to 2.565
S_6	37	−2.468 to 2.221	37	−1.234 to 1.234
S_5 (with $S_6=\frac{3}{5\sqrt{3}}S_5$)	21	−2.138 to 2.138	21	−2.138 to 2.138

lar geometry is kept planar, whereas in Fig. 3 the geometry is pyramidal ($S_2=-0.434$). If one compares the potential curves for the planar and pyramidal geometries, it becomes obvious that in the planar case there is only the JT coupling between the components of the E' states, whereas in the pyramidal case the PJT effect between the E'_x component and the ground state shows up. This is especially obvious if one compares the diabatic energies with the adiabatic ones in the figures. For planar displacements along S_5, there is hardly any coupling, while for the combined displacements of S_5 and S_6, a coupling originating from the JT effect becomes obvious. The potentials for the pyramidal displacements exhibit the PJT coupling between E' and the ground state by the deviation of the diabatic energies from the adiabatic energies. For energies up to 19 eV the fitted adiabatic energies show a sufficiently good agreement with the *ab initio* data. This is reflected by an overall rms fitting error for all parameters and data points of about 450 cm^{-1}. As already mentioned, this result is much better than it may appear. Noticeable deviations of the analytical representation from the *ab initio* data points are only found for large displacements and should have only a very limited influence on the accurate description of the nuclear dynamics studied in the following.

The surfaces are constructed in a way appropriate for bound-state calculations, which is the focus of the current study. Thus, the asymptotic behavior of the surfaces is not of interest as long as no exit channel is accessible at the energy of the wave packet. It is clear that due to the use of Taylor expansions for the potential matrix elements, the global surfaces may show oscillations or may be unbound in regions corresponding to very distorted geometries. For this reason, it was checked carefully that the potentials are devoid of open exit channels for energies at and well above the energy of the wave packet.

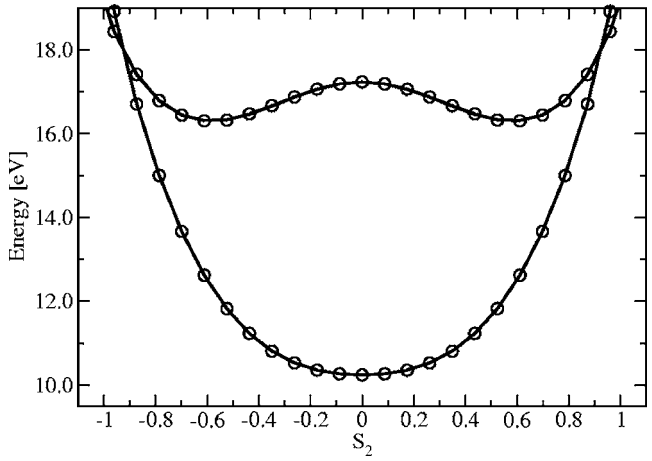

FIG. 1. Adiabatic energies (solid lines) as a function of the S_2 coordinate are compared to *ab initio* data (open circles).

III. DYNAMICAL INVESTIGATION

A. The method

The dynamics of NH_3^+ is described using the six mass weighted Cartesian normal modes $\boldsymbol{Q}=\{Q_1,\ldots,Q_6\}$ con-

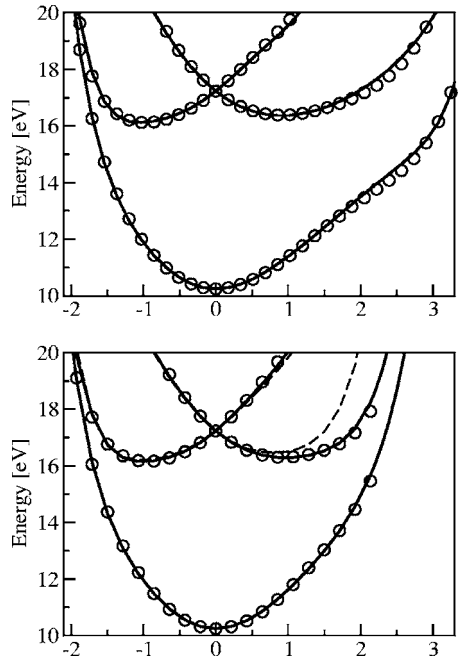

FIG. 2. Adiabatic (solid lines) and diabatic (dashed lines) energies (in eV) as a function of the S_5 coordinate (upper panel) and the combined S_5, S_6 $\left(S_6=\frac{3}{5\sqrt{3}}S_5\right)$ coordinates (lower panel, S_5 plotted) at planar geometry are compared to *ab initio* data (open circles).

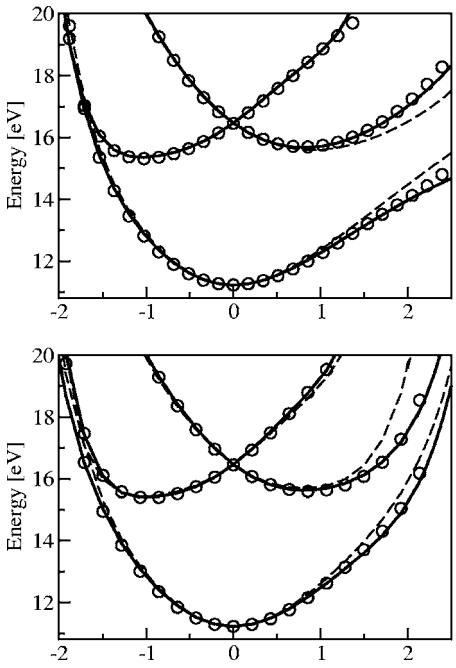

FIG. 3. Adiabatic (solid lines) and diabatic (dashed lines) energies (in eV) as a function of the S_5 coordinate (upper panel) and the combined S_5, S_6 $\left(S_6=\frac{3}{5\sqrt{3}}S_5\right)$ coordinates (S_5 plotted) at pyramidal geometry are compared to *ab initio* data (open circles).

structed at the equilibrium geometry of the ionic ground state (thus in D_{3h} symmetry). This choice ensures an equivalent description of the double wells in the umbrella mode which are present in the excited state of NH_3^+ and in neutral NH_3. Assuming that the mixed derivatives in the kinetic energy operator resulting from vibrational angular momenta can be neglected, the Hamiltonian for vanishing total angular momentum ($J=0$) reads

$$\hat{H} = -\frac{\hbar^2}{2}\sum_{i=1}^{6}\frac{\partial^2}{\partial Q_i^2}\mathbf{1} + \boldsymbol{V}(\mathbf{Q}), \tag{9}$$

where $\mathbf{1}$ is the 3×3 unity matrix and $\boldsymbol{V}(\mathbf{Q})$ is the diabatic 3×3 potential energy matrix. Computation of $\boldsymbol{V}(\mathbf{Q})$ requires the transformation, based on trigonometric considerations, from the normal modes $\boldsymbol{Q}$ to the symmetry-adapted coordinates $\boldsymbol{S}$.

The time evolution of the system after vertical ionization to the ground or the excited state of NH_3^+ is determined by wave packet propagations. Because of the comparatively high dimensionality and the expected ultrafast dynamics of this system, the MCTDH method[37,38] has been used. In the MCTDH approach, the wave function is represented in an optimized set of time-dependent basis functions, called single-particle functions, and the equations of motion are derived from the Dirac-Frenkel variational principle. For the present system, the MCTDH wave function reads

$$\psi(\boldsymbol{Q},t) = \sum_{n_1}\cdots\sum_{n_6}\sum_{\sigma=1}^{3} A_{n_1\cdots n_6\sigma}(t)\prod_{i=1}^{6}\phi_{n_i}^{(i)}(Q_i,t)\chi_\sigma, \tag{10}$$

where the $A_{n_1\cdots n_6\sigma}$ denote the time-dependent expansion coefficients and the $\phi_{n_i}^{(i)}$ the single-particle function in the nuclear coordinates. The χ_σ; $\sigma=1,2,3$ specify the diabatic electronic states. For the integration of the MCTDH equations of motion, a scheme similar to the one introduced by Beck and Meyer[39] is employed. To evaluate the matrix elements of the potential, the correlation discrete variable representation (CDVR) scheme[40] has been employed. It should be noted that the CDVR scheme is here employed to treat a diabatic potential matrix, while previously the CDVR scheme had only be used to treat single potential energy surfaces. The required generalization of the approach is straightforward. Details are described in Appendix D. For all six degrees of freedom, a Fourier basis set representation has been used for the representation of the time-dependent single-particle functions. Details of the wave function representation used are given in Table III.

During the MCTDH propagation, two quantities of interested are evaluated: the autocorrelation function and the adiabatic populations. The autocorrelation function $c(t)$, which is given by

$$c(t) = \langle\psi(t=0)|e^{-iHt}\psi(t=0)\rangle = \langle\psi^*(t/2)|\psi(t/2)\rangle, \tag{11}$$

gives access to the photoelectron spectral bands by Fourier transformation. To characterize the radiationless decay dynamics of the excited state of NH_3^+, the time evolution of the adiabatic population,

TABLE III. Details of the wave packet representation where for each of the normal modes described by their associated frequency and symmetry label, "range" indicates the limits of the box used (in a.u.), N the numbers of Fourier grid points, and n_A and n_E the numbers of single-particle functions used for the propagation after an excitation on the ground state and on the excited state of NH_3^+, respectively.

Mode	Description	Sym.	ω (cm^{-1})	Range	N	n_A	n_E
Q_1	Sym. stretch	a_1'	3428	[−68:67]	54	10	6
Q_2	Umbrella	a_2''	875	[−130:130]	64	10	18
Q_3	Asym. stretch	e'	3557	[−40:55]	32	4	7
Q_4	Asym. stretch	e'	3557	[−40:40]	32	4	7
Q_5	Asym. bending	e'	1592	[−100:110]	64	4	12
Q_6	Asym. bending	e'	1592	[−100:100]	64	4	12
Number of Hartree products						76 800	2 286 144

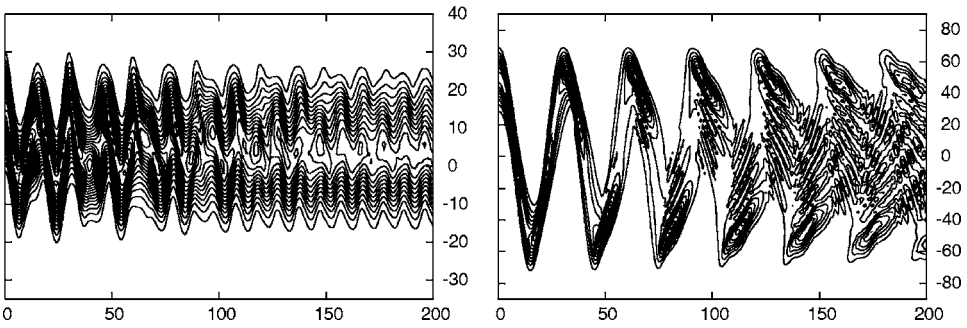

FIG. 4. Probabilities along Q_1 (left panel) and Q_2 (right panel), as a function of time in femtoseconds. a.u. have been used for the mass weighted normal modes.

$$P_\sigma^{(a)}(t) = \langle \psi(t) | \hat{P}_\sigma^{(a)} | \psi(t) \rangle, \quad \hat{P}_\sigma^{(a)} = |\chi_\sigma^{(a)}\rangle\langle\chi_\sigma^{(a)}|, \quad \sigma = 1,2,3, \tag{12}$$

is computed, where $\chi_\sigma^{(a)}$ are the adiabatic states obtained by diagonalization of the diabatic potential matrix for each grid point in the six-dimensional space

$$\underline{\chi}^{(a)} = U(\boldsymbol{Q})\underline{\chi}. \tag{13}$$

The CDVR scheme has been employed for the evaluation of the adiabatic projector matrix elements. We shall also consider the diabatic populations which are given by

$$P_\sigma^{(d)}(t) = \langle \psi(t) | \hat{P}_\sigma^{(d)} | \psi(t) \rangle, \quad \hat{P}_\sigma^{(d)} = |\chi_\sigma\rangle\langle\chi_\sigma|, \quad \sigma = 1,2,3. \tag{14}$$

In order to have a better insight into the evolution of the wave packet, the probability densities for each coordinate, defined as the integral of the absolute square of the nuclear wave function over all remaining nuclear coordinates and summed over all electronic states, are also computed.

The initial wave packet used for the computation of the two photoionization bands is taken to be the localized (with respect to inversion) vibrational ground state of neutral NH_3. It corresponds to a superposition of the two essentially degenerate lowest-energy levels which are both populated in the experiment. The localized vibrational ground state of NH_3 is numerically determined by a MCTDH propagation in imaginary time. The propagation time is tuned to remove from the initial guess all excitations except the tunneling splitting, resulting in a propagation time of 827.24 a.u. The energy of the initial state is 0.8707 eV above the minimum of the neutral potential surface. This corresponds to 91% of the zero-point energy in the harmonic approximation. From this starting wave packet, the two photoionization bands are separately computed by a vertical ionization onto the ground and one of the two excited states of NH_3^+.

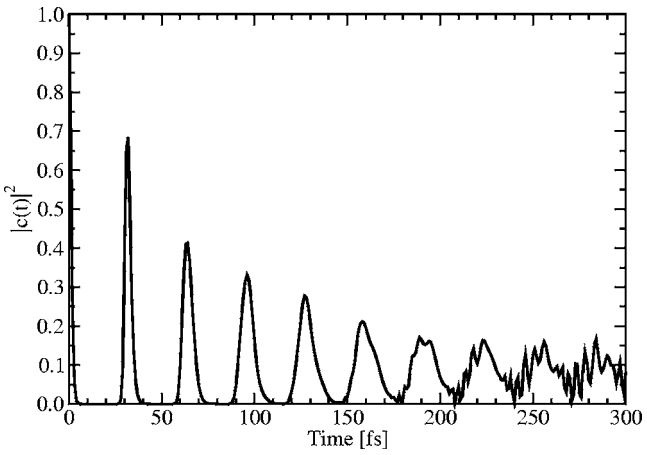

FIG. 5. Modulus square of the autocorrelation function $|c(t)|^2$ up to 300 fs.

B. Ionization to the ground state

The time evolution of the wave packet after instantaneous vertical ionization from the neutral NH_3 surface to the ground state of NH_3^+ can be monitored by the inspection of the probabilities along the six nuclear coordinates. The probabilities along the two relevant coordinates, that is the umbrella coordinate Q_2 and the totally symmetric stretching coordinate Q_1, are presented in Fig. 4 up to 200 fs. For both coordinates, the wave packet presents strong oscillations. Along the four other coordinates, only small variations in amplitude are observed. The damped oscillations, observed along the stretching coordinate Q_1 for at least 50 fs and along the umbrella mode Q_2 for at least 100 fs, are responsible of the recurrences in the autocorrelation function presented in Fig. 5. The autocorrelation function decays to zero in 5 fs and exhibits a first recurrence at 32 fs, followed by a series of six exponentially attenuated recurrences. The attenuation as well as the asymmetric shape of the recurrences are due to the anharmonicity present in the potential energy surface. Figure 6 compares the low-energy part of the experimental photoelectron spectrum of NH_3 with the computed spectrum obtained after ionization to the ground state of NH_3^+. The spectrum has been computed by Fourier transfor-

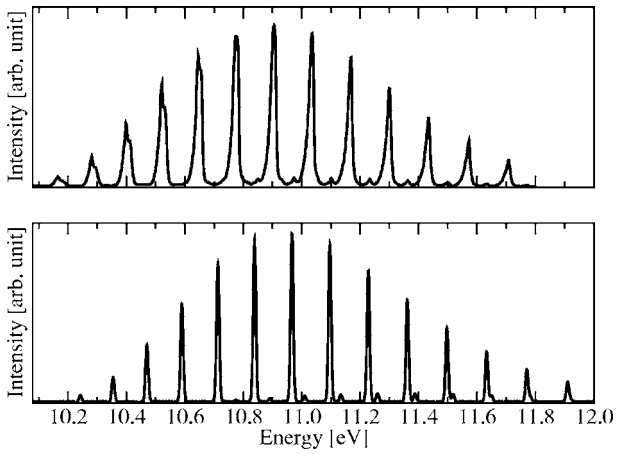

FIG. 6. First band of the photoelectron spectrum of NH_3: experimental spectrum from Ref. 5 (top panel) and present result (bottom panel).

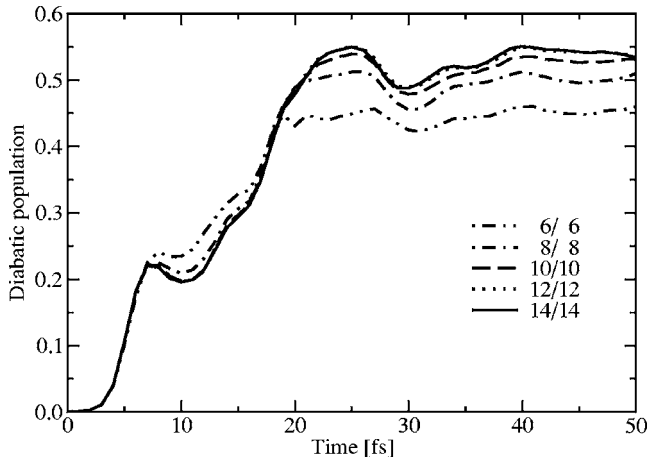

FIG. 7. Evolution of the population probability of the diabatic χ_1 state (lowest in energy at the reference geometry) for different numbers of single-particle functions employed for the asymmetric bending modes Q_5 and Q_6.

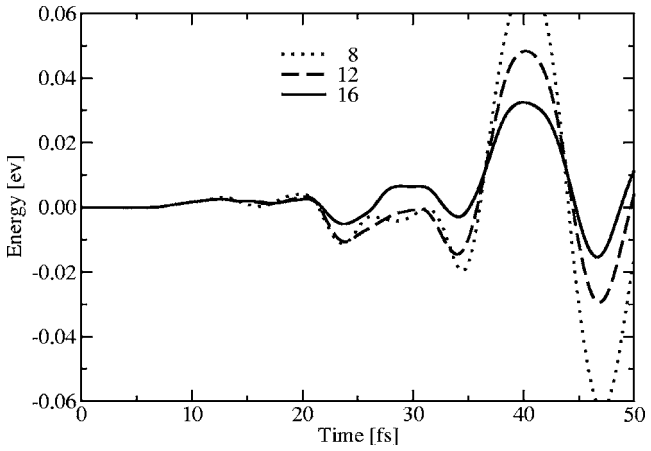

FIG. 8. Evolution of the energy of the wave packet (relative to its initial value in eV) after ionization to one of the diabatic excited states of NH_3^+ for different numbers of single-particle functions employed for the umbrella mode Q_2.

mation of the autocorrelation function. The basis set used to propagate the wave packet for 200 fs is given in Table III. To avoid spurious oscillations due to the finite propagation time, a Gaussian damping factor, $\exp(-t^2/t_{\mathrm{damp}}^2)$ with $t_{\mathrm{damp}}=200$ fs, has been employed. The main vibrational progression of the band is accurately reproduced by our calculations. The computed 0–0 line position is 10.242 eV. The experimental 0–0 line,[5] found at 10.242 eV, is only 0.056 eV lower than our calculation. For both the experimental and the theoretical spectra, the maximum of the progression occurs for the 0–6 line. A secondary progression is present in both spectra. From the inspection of the wave packet evolution as well as of the harmonic frequencies of the different modes, the second progression is assigned to an excitation of the symmetric stretch mode ν_1.

No transfer of population is observed and after 200 fs of propagation time, the ground state adiabatic population is 0.997.

C. Ionization to the excited state

1. Convergence considerations

The larger energy range available to the wave packet after ionization onto one of the two equivalent excited diabatic states induces a more delicate computation for which the convergence is not straightforward. Therefore, a systematic and thorough check of the convergence with respect to the definition and size of the MCTDH basis set has been performed. The major test consists in a systematic increase of the number of single-particle functions for each of the six coordinates until both the adiabatic population and the spectrum (computed from the autocorrelation function) have been found to be unaffected by further increases. Additionally, the energy of the wave packet has been monitored. While the energy is, in principle, a constant of the MCTDH equations of motion, the CDVR quadrature can violate the conservation of energy if an insufficient number of single-particle functions is employed. Thus, the conservation of energy can be used to monitor inaccuracies of the CDVR quadrature.[41]

Figure 7 displays a typical convergence behavior observed for the diabatic population probability. The populations have been computed with an increasing number of single-particle functions for the asymmetric bending modes Q_5 and Q_6 (from 6 to 14 per mode), keeping the number of single-particle functions for the other modes constant. The corresponding basis set sizes correspond to 139 968 Hartree products for the smallest and to 762 048 for the biggest basis. Examination of the figure shows that 12 single-particle functions for Q_5 and Q_6 are enough to converge the population up to 50 fs. The convergence behavior of the ground state adiabatic population has been found to be identical. Similar convergence studies for the other modes lead to the final basis set size given in Table III. Note that the underlying primitive grid, converged for the most energetic study, has been kept identical for the calculation of both bands.

An example of the deviation of the wave packet energy from the initial value as a function of time is shown in Fig. 8. The calculations presented correspond to a systematic increase of the number of single-particle functions used for the umbrella normal mode Q_2, keeping the numbers used for the other modes constant. It can be seen that the nonconservation of the total energy due to the use of the CDVR scheme is directly related to the basis set size. A systematic improvement of the energy conservation is obtained by increasing the basis set size. For the largest computation, for which the basis set size is given in Table III, the largest variation of the energy has been found to be 0.02 eV (thus less than 0.3% of the available energy).

2. Wave packet evolution

Probability densities for each coordinate monitoring the time evolution of the wave packet after instantaneous vertical ionization from the neutral NH_3 surface to either of the excited diabatic states of NH_3^+ are presented in Fig. 9. As expected from the PE shape, the initial motion of the wave packet corresponds to an elongation of the NH bonds, as seen in Fig. 9(a) (note that the definition of Q_1 is such that negative Q_1 correspond to bond elongation) and a closing of the umbrella angle [Fig. 9(b)]. The quasiperiodic oscillatory motion along Q_1 with a frequency of 12–13 fs is rapidly damped due to the intrinsic nonseparability of the potential

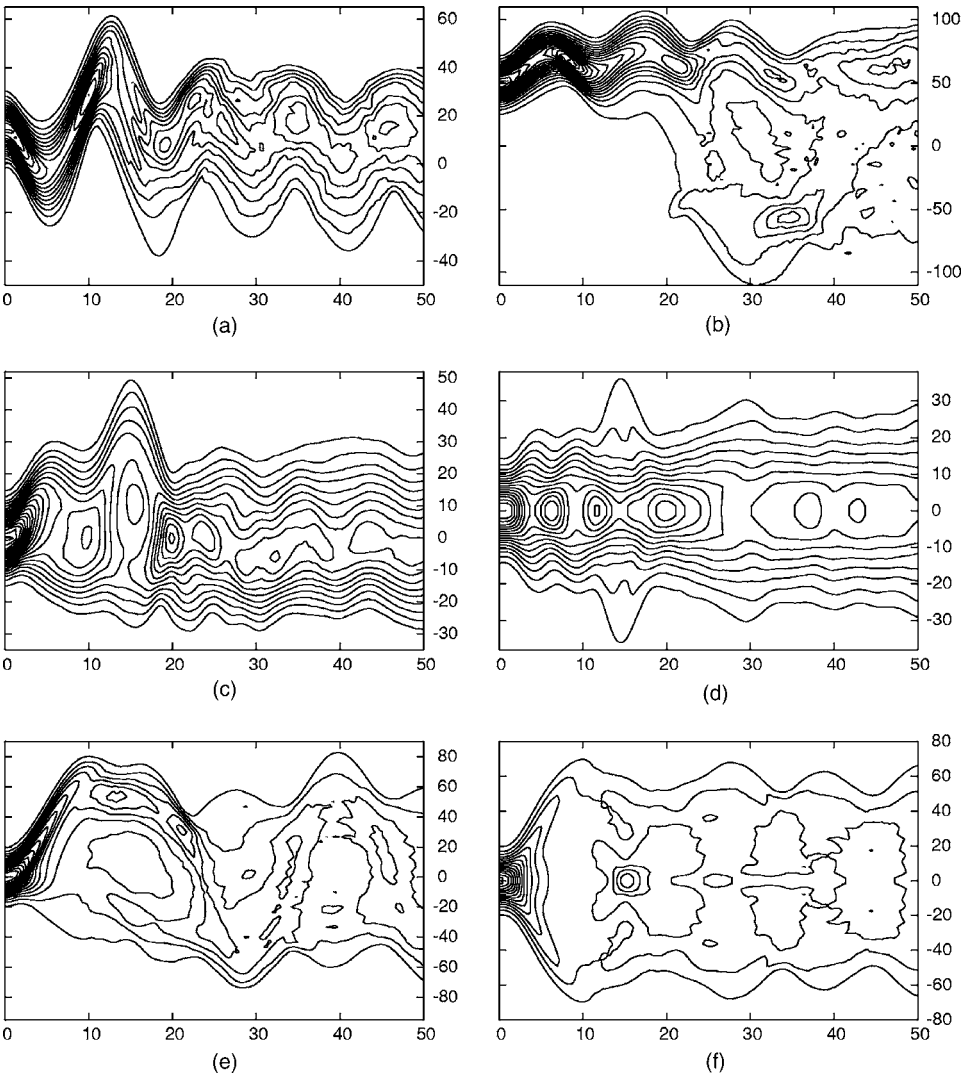

FIG. 9. Probabilities for the six coordinates (a) Q_1, (b) Q_2, (c) Q_3, (d) Q_4, (e) Q_5, and (f) Q_6, as a function of time in femtoseconds. a.u. have been used for the mass weighted normal modes.

surfaces. It takes slightly more than 20 fs for the molecule to reach planarity ($Q_2=0$), as seen in Fig. 9(b). 30 fs are sufficient for the wave packet to sample geometries corresponding to the inversion of the pyramidalization angle with respect to $t=0$. As is obvious from the electronic populations evolution (see below), this is related to the fact that a nonnegligible part of the wave packet has reached the ground state of NH_3^+ which has a single well along the umbrella mode. Evolution of the wave packet along the asymmetric stretching modes (Q_3 and Q_4), presented in Figs. 9(c) and 9(d), is characterized by a moderate spreading superimposed on a damped oscillatory behavior. A much more pronounced spreading and damping is observed for the asymmetric bending modes (Q_5 and Q_6), presented in Figs. 9(e) and 9(f). Localization of the wave packet, especially along the umbrella mode, is lost as early as after a 30 fs propagation time. The dynamics of NH_3^+ can be described to be composed of two steps. During the initial very fast step, the localized wave packet follows the gradient along all six modes and performs one oscillation in one of the double wells along the umbrella mode. This is accompanied by a loss of the C_3 symmetry. An efficient nonadiabatic coupling between the surfaces induces a transfer of the wave packet onto the ground state. In the second step, the dynamics is mostly determined by the ground state surface with a large vibrational excess energy.

3. Photoelectron spectra

Figure 10 (bottom) shows the photoionization spectrum

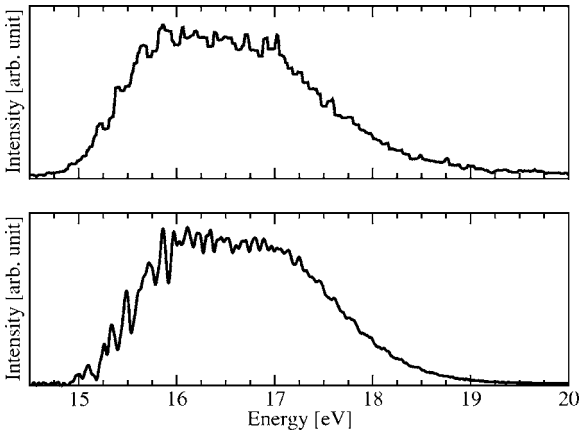

FIG. 10. Second band of the photoelectron spectrum of NH_3: experimental spectrum from Ref. 5 (top panel) and present result (bottom panel).

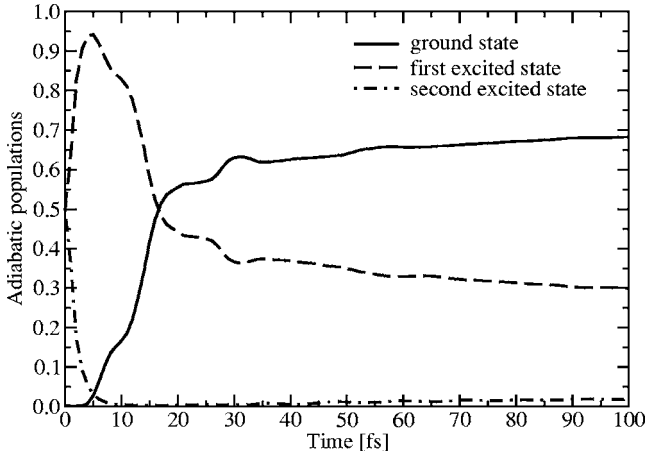

FIG. 11. Adiabatic electronic population of the ground and excited states of NH_3^+ after excitation into one of the diabatic excited state, as a function of time in femtoseconds. The basis set size used is given in Table III.

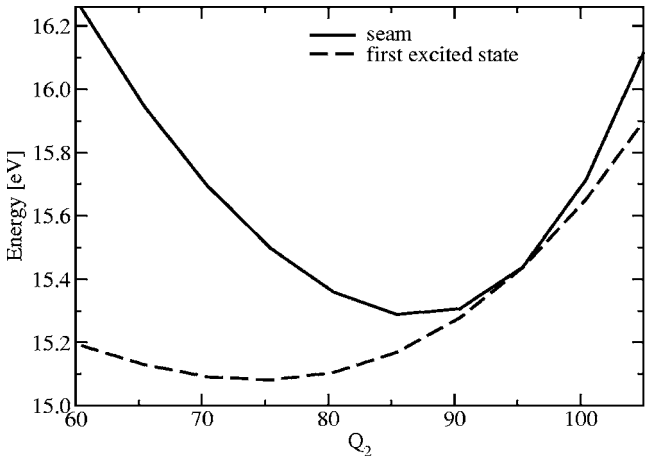

FIG. 12. Energy (eV) of the minimum of the intersection seam between the ground and first excited states (straight line) and of the minimum of the first excited state (dashed line) as a function of the umbrella coordinate Q_2.

obtained after excitation of the wave packet to the diabatic ^2E excited state of NH_3^+. The spectrum has been calculated from the autocorrelation function up to a time $t=100$ fs, using $t_{\mathrm{damp}}=75$ fs to damp the autocorrelation function. The details of the basis set used are given in Table III.

In contrast to the well-resolved vibrational progression found for the ionic ground state, ionization to the first excited state of NH_3^+ results in a broad, congested spectrum with very little structure. The onset of this band is located slightly below 15 eV and it extends up to roughly 19 eV. The widths and the overall shape of this spectrum are reproduced in excellent agreement with the measurement. The theoretical spectrum shows a slightly more pronounced structure near the low-energy edge of the band. This may be due to the choice of the damping time t_{damp} of the autocorrelation function and should not be overinterpreted. The experimental band starts with a steep increase of intensity in which five poorly resolved features can be recognized, the first one around 15 eV only being a weak shoulder. This behavior is well reproduced by the calculated spectrum, though the first two features are resolved double peaks. Between roughly 16 and 17 eV the intensity of the band shows a plateau with a number of weak peaks. It is not possible to match these features line by line because the uncertainties from the experimental resolution and the accuracy of the calculation are too large. After 17 eV, the intensity of the band decays in an approximately exponential manner.

4. Population dynamics

The evolution of the adiabatic populations after ionization to the excited state is presented in Fig. 11 up to 100 fs. This evolution of population consists of three time scales. Within about 5 fs, the population of the highest adiabatic state decreases from one-half to nearly zero and the middle adiabatic state reaches a population of about 0.95. This initial decay from the highest to the middle adiabatic state reflects the ultrafast Jahn-Teller dynamics within the two excited states of the ammonia cation. The further decay to the ground state of the ammonia cation starts at about 4 fs. Two different time scales are found for this internal conversion (IC). In a fast first step, more than half of the population is transferred to the ground adiabatic state within the first 20 fs. This fast initial IC is followed by a slow one which is not completed even within the 100 fs time period studied in the present work.

Extrapolating the present data, a tentative time scale in the picosecond range can be inferred from Fig. 11. The fast decay within the first 20 fs can clearly be assigned to wave packet components which reach the conical intersection between the ground and middle adiabatic PES directly within the first vibrational period. This part constitutes 50%–60% of the complete wave packet, presumably predominately its higher-energy components. However, a sizable fraction of the wave packet cannot access the conical intersection directly. Its decay to the ground state surface is comparatively slow and seems to be better described as a statistical rate process.

To illustrate this situation, Fig. 12 presents the minimal energy of the middle adiabatic PES and of the seam of intersection for given values of the umbrella coordinate Q_2. These energy values are obtained by minimizing the respective energy with respect to all other coordinates except Q_2 (including also the additional constrains if the seam of intersection is considered). It should be noted that for a given value of the umbrella coordinate the optimal geometries for the minimal energy of the middle adiabatic PES and of the seam of intersection differ.

The comparison of the energy minimum of the seam (15.28 eV) with the energy of the wave packet (see Fig. 10) indicates that the seam is energetically reachable. However, the minima of the two curves in Fig. 12 are located at significantly different geometries. Since the wave packet spreads after an initial relaxation period mostly in the valley of the PES (as can be understood from statistical mechanical arguments), only its tails will reach the conical intersection. Thus, after a fast initial decay of the higher-energy components, only small parts of the wave packet reach the conical intersection within a given period of time and the wave packet will be partially dynamically caught in the local minimum of the middle adiabatic state.

The overall behavior observed is similar to the diabatic population evolution given in Ref. 11, leading to the conclusion that a very efficient coupling to the ground state induces an ultrafast transfer of electronic population. However, some differences are notable. The population obtained in the present work exhibits much less oscillations than the one previously published, and the increase of population starts slightly later. Analysis of the diabatic population evolution obtained in the present work reveals more oscillations and a slightly earlier increase of the ground state population, but the differences with the diabatic populations of Ref. 11 remain.

IV. CONCLUSIONS

The photoelectron spectrum of ammonia has been studied by full-dimensional time-dependent quantum dynamics calculations on a newly developed set of coupled PESs for NH_3^+. The analytic representation of the three PESs, corresponding to the $\tilde{X}\,^2A_2''$ and the $\tilde{A}\,^2E'$ states of NH_3^+, is based on polynomial expansions of the diabatic PE matrix elements in symmetry coordinates. It includes higher-order Jahn-Teller and pseudo-Jahn-Teller couplings and accounts for the strong anharmonicity of the potentials. The model also reproduces the dependence of the PJT coupling on the umbrella coordinate. This is of great importance because the PJT coupling vanishes for planar configurations. The expansion coefficients of the PE matrix elements have been determined by fitting of adiabatic energies along all coordinates obtained by highly accurate MRCI calculations. A relatively small number of *ab initio* points have been used in this work both because the Taylor expansions used are well behaved and fairly coarse grids are sufficient to determine the corresponding parameters. Also, only limited mode-mode coupling terms have been included in the model. Thus, extensive combined displacement grids are not mandatory.

The nonadiabatic dynamics of the system has been studied by accurate quantum wave packet propagations, using the efficient MCTDH method. These calculations have been performed in mass-scaled Cartesian normal coordinates. Thus, a nonlinear coordinate transformation and the use of the CDVR scheme for the potential evaluation are required. Vibrational angular momenta in the kinetic energy have been neglected.

The first two bands of the photoelectron spectrum have been determined from the autocorrelation function, resulting from wave packet propagations. Both calculated bands are in excellent agreement with the experiment and are of fundamentally different character. The band corresponding to the $\tilde{X}\,^2A_2''$ state of NH_3^+ shows a well-resolved progression which is due to the umbrella vibration. In agreement with the experiment, the maximum intensity is observed for the 0-6 transition. A weak secondary progression is seen which is due to the symmetric stretching mode.

In contrast to the first band of the spectrum, the band corresponding to the $\tilde{A}\,^2E'$ state is completely congested and no resolved progression can be identified. The band shape is characterized by a rapid onset around 15 eV, a plateau between roughly 15.5 and 17 eV, followed by an exponential decay. The absence of resolved transitions is due to the strong vibronic coupling within the $^2E'$ state and the PJT coupling to the electronic ground state. The latter coupling is also responsible for a very rapid radiationless decay of the excited state. This has been studied by determination of the time evolution of the adiabatic populations. It is found that after ionization to the $^2E'$ state, the wave packet decays very rapidly to the ground state with essentially no recurrences to the excited state. Most of this decay is finished within as little as 20 fs, which provides a qualitative explanation of the absence of fluorescence in the experiments. However, the calculated decay is incomplete, and roughly a third of the population remains on the excited state surfaces. The partial decay is understood as a statistical effect induced by the location of the intersection seam far from the local minimum of the first excited state where parts of the wave packet are temporarily captured.

The neglect of vibrational angular momenta when using the Cartesian normal modes for the dynamical computations is a clear limitation of the presented work, especially when large displacements are involved. Work investigating the accuracy of this approximation is in progress.

ACKNOWLEDGMENTS

Four of the authors (A.V., W.E., S.N., and W.D.) acknowledge financial support of the Bayerisch-Französisches Hochschulzentrum—Centre de Coopération Franco-Bavarois. One of the authors (U.M.) acknowledges support by the Sonderforschungsbereich 613 of the Deutsche Forschungsgemeinschaft. The authors are thankful to COST (Project No. D26/0006/02 "Dynamics of nonadiabatic processes") and to the Chemistry Department of the CNRS (France) for additional financial support. The Deutsche Forschungsgemeinschaft and the Fonds der Chemischen Industrie are gratefully acknowledged for financial support. Large amounts of computing time have been generously provided by the Leibniz Rechenzentrum.

APPENDIX A: EXPLICIT EXPRESSION FOR $\mathcal{V}_A^{(7)}$ AND $\mathcal{V}_A^{(8)}$

The derivation of the seventh and eighth order terms of the $\mathbf{V}^{\mathrm{diag}}$ matrix is done as explained in Refs. 30 and 31. In the complex representation, the nonvanishing diagonal terms of the Hamiltonian ($H_{aa}=H_{++}=H_{--}$) are $Q_+^5Q_-^2$ and $Q_+^2Q_-^5$ for the seventh order and $Q_+^7Q_-^1$, $Q_+^4Q_-^4$ and $Q_+^1Q_-^7$ for the eighth order. Transformation to the real coordinates and electronic basis sets leads to the explicit expressions used in this work

$$\mathcal{V}^{(7)} = a_1^{(7)}[2x^7 - 2x^5y^2 - 10x^3y^4 - 6xy^6], \tag{A1a}$$

TABLE IV. Potential energy (eV) of NH_3 ground state and NH_3^+ states for the reference geometry $q_i=0$, $i=1,\ldots,6$. The minimum of NH_3 is taken as the origin for energies.

Species	State	Energy (eV)
NH_3	$^1A_1$	0.323
NH_3^+	$^2A_2''$	10.243
NH_3^+	$^2E'$	17.231

TABLE V. Parameters (a.u.) of S_1 and S_2 parts of the fitted surfaces of NH_3^+.

		S_1		
j	r_j	α_j	$D_j^{(2)}$	$D_j^{(3)}$
A	0.001 274	0.517 395	0.836 990	−0.209 334
E	0.206 476	0.529 754	0.586 548	−0.131 633
		S_2		
j	$u_j^{(1)}$	$u_j^{(2)}$	$u_j^{(3)}$	$u_j^{(4)}$
A	0.269 017	8.097 2	−167.709	5064.58
E	−0.446 702	10.537 0	−194.259	4929.76

$$\mathcal{V}^{(8)} = a_1^{(8)}[2x^8 - 28x^6y^2 + 28x^2y^6 - 2y^8] + a_2^{(8)}[x^8 + 4x^6y^2 + 6x^4y^4 + 4x^2y^6 + y^8]. \quad \text{(A1b)}$$

APPENDIX B: SIX-DIMENSIONAL THREE-SHEETED PES OF NH_3^+

Additionally to the vertical excitation energies given in Table IV, the analytical three-sheeted PES for the lowest electronic states of NH_3^+ contains 77 parameters which are given in Tables V–VIII.

APPENDIX C: SIX-DIMENSIONAL PES OF NH_3

In order to model the initial wave packet, a six-dimensional analytical fit of the electronic ground state surface of neutral NH_3 has been derived. The following simple and separable analytical form used respects the D_{3h} symmetry operations

$$V(\boldsymbol{S}) = D^{(2)}\{1-\exp[\alpha(r-S_1)]\}^2 + D^{(3)}\{1-\exp[\alpha(r-S_1)]\}^3 - D^{(2)}\{1-\exp[\alpha r]\}^2 - D^{(3)}\{1-\exp[\alpha r]\}^3 + \sum_{n=1}^{4}\frac{u^{(n)}}{(2n)!}S_2^{2n} + \sum_{n=0}^{6}\frac{1}{n!}\mathcal{V}^{(n)}(S_3,S_4,\mathbf{a}^{(n)}(3)) + \sum_{n=0}^{6}\frac{1}{n!}\mathcal{V}^{(n)}(S_5,S_6;\mathbf{a}^{(n)}(5)). \quad \text{(C1)}$$

The corresponding parameters are given in Tables IX and X.

TABLE VII. JT and PJT parameters (a.u.) of the S_3 and S_4 parts of the fitted surfaces of NH_3^+.

n	$\lambda_1^{(n)}$ (JT,3)	$\lambda_2^{(n)}$ (JT,3)	$\lambda_1^{(n)}$ (PJT,3)	$\lambda_2^{(n)}$ (PJT,3)
1	0.062 946	⋯	0.034 477 5	⋯
2	0.022 238 4	⋯	0.095 851 4	⋯
3	−0.005 552 97	⋯	0.318 965	⋯
4	−0.254 622	0.311 172	−0.410 166	−1.485 67
5	0.238 335	−2.778 57	1.811 58	−3.700 9
6	18.932 8	−16.336 5	⋯	⋯

APPENDIX D: THE CDVR APPROACH FOR AN EXTENDED CLASS OF HAMILTONIAN OPERATORS

In the original work introducing the CDVR approach,[40] Hamiltonian operators of the form

$$\hat{H} = \sum_{m=1}^{M} \hat{h}_m^{(1)}\hat{h}_m^{(2)}\cdots\hat{h}_m^{(f)} + V(x_1,x_2,\ldots,x_f) \quad \text{(D1)}$$

have been considered. Here each of the operators $\hat{h}_m^{(\kappa)}$ acts only on the κth coordinate and f denotes the total number of degrees of freedom. In applications studying the dynamics on a single electronic potential energy surface, the first term in the sum of Eq. (D1) usually represents the kinetic energy operator and the second term, $V(x_1,x_2,\ldots,x_f)$, is the potential function. Then the CDVR approach facilitates straightforward MCTDH wave function propagation for arbitrary potentials $V(x_1,x_2,\ldots,x_f)$ without requiring to represent the potential in the form

$$V = \sum_{j=1}^{J} v_j^{(1)}(x_1)v_j^{(2)}(x_2)\cdots v_j^{(f)}(x_f). \quad \text{(D2)}$$

If the quantum dynamics on multiple coupled potential energy surfaces is studied, multiple potentials and potential couplings have to be considered. Except for favorable cases, where the potentials are simply structured or can be reexpanded in the form of Eq. (D2), the Hamiltonian can then not be written in the form of Eq. (D1). An extended version of the CDVR approach is required and will be described in the following.

TABLE VI. Parameters (a.u.) of the diagonal part $\mathbf{V}^{\text{diag}}$ involving asymmetric modes S_3, S_4, S_5, and S_6, of the surfaces of NH_3^+. Note that the vertical energies are in the constant $\mathbf{V}^{(0)}$ matrix of Eq. (1).

	S_3,S_4				S_5,S_6			
n	$a_1^{(n)}$ $(A,3)$	$a_2^{(n)}$ $(A,3)$	$a_1^{(n)}$ $(E,3)$	$a_2^{(n)}$ $(E,3)$	$a_1^{(n)}$ $(A,5)$	$a_2^{(n)}$ $(A,5)$	$a_1^{(n)}$ $(E,5)$	$a_2^{(n)}$ $(E,5)$
0	0	⋯	0	⋯	0	⋯	0	⋯
1	⋯	⋯	⋯	⋯	⋯	⋯	⋯	⋯
2	0.434 568	⋯	0.434 136	⋯	0.109 886	⋯	0.078 518 8	⋯
3	−0.276 748	⋯	−0.266 733	⋯	−0.028 439 8	⋯	−0.033 637 7	⋯
4	2.311 920	⋯	1.942 73	⋯	−0.129 60	⋯	−0.191 92	⋯
5	−3.393 050	⋯	−3.284 13	⋯	0.078 025 7	⋯	0.174 633	⋯
6	0.947 091	12.9584	1.450 65	15.1244	0.076 723 4	0.889 354	0.039 051	2.648 31
7	⋯	⋯	⋯	⋯	−2.043 14	⋯	⋯	⋯
8	⋯	⋯	⋯	⋯	0.576 692	3.792 38	⋯	⋯

TABLE VIII. JT and PJT parameters (a.u.) of the S_5 and S_6 parts of the fitted surfaces of NH_3^+.

n	$\lambda_1^{(n)}$ (JT,5)	$\lambda_2^{(n)}$ (JT,5)	$\lambda_1^{(n)}$ (PJT,5)	$\lambda_2^{(n)}$ (PJT,5)
1	0.074 833 5	⋯	0.053 636 5	⋯
2	−0.019 310 2	⋯	−0.004 461 74	⋯
3	−0.038 387 2	⋯	−0.005 287 06	⋯
4	−0.098 389 1	−0.069 028 3	−0.066 454 8	0.021 087 4
5	−0.016 843 3	0.342 386	0.085 104 1	0.096 330 9
6	1.954 49	0.727 939	0.174 926	−0.326 13

TABLE IX. Parameters (a.u.) of S_1 and S_2 parts of the fitted ground state surface of NH_3.

		S_1	
r	α	$D^{(2)}$	$D^{(3)}$
−0.081 044 6	0.525 422	0.900 567	−0.210 640
		S_2	
$u^{(1)}$	$u^{(2)}$	$u^{(3)}$	$u^{(4)}$
−0.267 538	11.542 5	−235.221	5894.67

The CDVR approach can be straightforwardly extended to Hamiltonian operators of the form

$$\hat{H} = \sum_{n=1}^{N} \hat{H}_n,$$

$$\hat{H}_n = V_n(x_1, x_2, \ldots, x_{z_n}) \hat{h}_n^{(z_n+1)} \hat{h}_n^{(z_n+2)} \cdots \hat{h}_n^{(f)}. \tag{D3}$$

[Note that Eq. (D1) is a special case of the above equation with $N=M+1$, $V_n=1$, $z_n=0$ for $n=1,2,\ldots,M$, and $V_{M+1}=V$, $z_{M+1}=0$.] The Hamiltonian used in the present work can be written in the form of Eq. (D1). It then reads

$$\hat{H} = \sum_{n=1}^{6} -\frac{1}{2}\frac{\partial^2}{\partial Q_n^2} + \sum_{n=7}^{12} V_n(Q_1, Q_2, \ldots, Q_6) \hat{h}_n^{(7)}, \tag{D4}$$

where the V_n denote the diabatic potentials and potential couplings and the operators $\hat{h}_n^{(7)}$ are the corresponding matrices

$$\begin{pmatrix} 1 & 0 & 0 \\ 0 & 0 & 0 \\ 0 & 0 & 0 \end{pmatrix}, \quad \begin{pmatrix} 0 & 0 & 0 \\ 0 & 1 & 0 \\ 0 & 0 & 0 \end{pmatrix}, \quad \begin{pmatrix} 0 & 0 & 0 \\ 0 & 0 & 0 \\ 0 & 0 & 1 \end{pmatrix}, \quad \begin{pmatrix} 0 & 1 & 0 \\ 1 & 0 & 0 \\ 0 & 0 & 0 \end{pmatrix}, \quad \begin{pmatrix} 0 & 0 & 1 \\ 0 & 0 & 0 \\ 1 & 0 & 0 \end{pmatrix}, \quad \begin{pmatrix} 0 & 0 & 0 \\ 0 & 0 & 1 \\ 0 & 1 & 0 \end{pmatrix}, \tag{D5}$$

acting on the electronic degree of freedom.

The modifications required in the calculation of the matrix elements of the Hamiltonian,

$$\langle \phi_{i_1}^{(1)} \cdots \phi_{i_f}^{(f)} | \hat{H} | \phi_{j_1}^{(1)} \cdots \phi_{j_f}^{(f)} \rangle = \sum_{n=1}^{N} \langle \phi_{i_1}^{(1)} \cdots \phi_{i_f}^{(f)} | \hat{H}_n | \phi_{j_1}^{(1)} \cdots \phi_{j_f}^{(f)} \rangle, \tag{D6}$$

and the single-hole matrices,

$$\langle \hat{H} \rangle_{ij}^{(\kappa)} = \sum_{n=1}^{N} \langle \hat{H}_n \rangle_{ij}^{(\kappa)} \tag{D7}$$

(for a detailed definition of symbols and nomenclature the reader is referred to Refs. 38 and 40) are rather obvious and only the final results will be given here. The contributions to the matrix elements resulting for a term $\hat{H}_n$ in the Hamiltonian are computed using the (time-dependent) grid representation $|q_{i_\kappa}^{(\kappa)}\rangle$ in the coordinates $x_1, x_2, \ldots, x_{z_n}$ and the (time-dependent) basis representation $|\phi_{i_\kappa}^{(\kappa)}\rangle$ in the coordinates $x_{z_n+1}, x_{z_n+2}, \ldots, x_f$,

$$\begin{aligned} &\langle q_{i_1}^{(1)} \cdots q_{i_{z_n}}^{(z_n)} \phi_{i_{z_n+1}}^{(z_n+1)} \cdots \phi_{i_f}^{(f)} | H_n(x_1, \ldots, x_{z_n}) \\ &\quad | q_{j_1}^{(1)} \cdots q_{j_{z_n}}^{(z_n)} \phi_{j_{z_n+1}}^{(z_n+1)} \cdots \phi_{j_f}^{(f)} \\ &= \langle \phi_{i_{z_n+1}}^{(z_n+1)} | \hat{h}_n^{(z_n+1)} | \phi_{j_{z_n+1}}^{(z_n+1)} \rangle \cdots \langle \phi_{i_f}^{(f)} | \hat{h}_n^{(f)} | \phi_{j_f}^{(f)} \rangle \\ &\quad \times \langle q_{i_1}^{(1)} \cdots q_{i_{z_n}}^{(z_n)} | V_n(x_1, \ldots, x_{z_n}) | q_{j_1}^{(1)} \cdots q_{j_{z_n}}^{(z_n)} \rangle, \end{aligned} \tag{D8}$$

where

TABLE X. Parameters (a.u.) of part of the NH_3 ground electronic state involving asymmetric modes S_3, S_4, S_5, and S_6.

	S_3, S_4		S_5, S_6	
n	$a_1^{(n)}(3)$	$a_2^{(n)}(3)$	$a_1^{(n)}(5)$	$a_2^{(n)}(5)$
2	0.423 246	⋯	0.099 789 7	⋯
3	−0.312 853	⋯	−0.027 624	⋯
4	2.458 25	⋯	−0.033 151 4	⋯
5	−1.227 02	⋯	−0.038 537 2	⋯
6	0.467 848	0.054 733 9	0.052 212 7	0.279 073

$$\langle q_{i_1}^{(1)} \cdots q_{i_{z_n}}^{(z_n)} | V_n(x_1, \ldots, x_{z_n}) | q_{j_1}^{(1)} \cdots q_{j_{z_n}}^{(z_n)} \rangle$$
$$= (V(q_{i_1}^{(1)}, \ldots, q_{i_{z_n}}^{(z_n)}) \delta_{i_1 j_1} \cdots \delta_{i_{z_n} j_{z_n}}$$
$$+ \sum_{\kappa=1}^{z_n} \langle q_{i_\kappa}^{(\kappa)} | \Delta V(q_{i_1}^{(1)}, \ldots, q_{i_{\kappa-1}}^{(\kappa-1)}, x_\kappa, q_{i_{\kappa+1}}^{(\kappa+1)}, \ldots, q_{i_{z_n}}^{(z_n)}) | q_{j_\kappa}^{(\kappa)} \rangle$$
$$\times \delta_{i_1 j_1} \cdots \delta_{i_{\kappa-1} j_{\kappa-1}} \delta_{i_{\kappa+1} j_{\kappa+1}} \cdots \delta_{i_{z_n} j_{z_n}}), \tag{D9}$$

are the usual CDVR potential matrix elements with

$$\langle q_{i_\kappa}^{(\kappa)} | \Delta V(q_{i_1}^{(1)}, \ldots, q_{i_{\kappa-1}}^{(\kappa-1)}, x_\kappa, q_{i_{\kappa+1}}^{(\kappa+1)}, \ldots, q_{i_{z_n}}^{(z_n)}) | q_{j_\kappa}^{(\kappa)} \rangle$$
$$= \langle q_{m_\kappa}^{(\kappa)} | V(q_{i_1}^{(1)}, \ldots, q_{i_{\kappa-1}}^{(\kappa-1)}, x_\kappa, q_{i_{\kappa+1}}^{(\kappa+1)}, \ldots, q_{i_{z_n}}^{(z_n)}) | q_{j_\kappa}^{(\kappa)} \rangle$$
$$- V(q_{i_1}^{(1)}, \ldots, q_{i_{z_n}}^{(z_n)}) \delta_{i_\kappa j_\kappa}. \tag{D10}$$

The contributions to the single-hole matrices $\langle \hat{H}_n \rangle^{(\kappa)}$ are computed using a MCTDH coefficient vector $\tilde{A}$ transformed to the (time-dependent) grid representation in the coordinates $x_1, x_2, \ldots, x_{\kappa-1}, x_{\kappa+1}, \ldots, x_{z_n}$ (excluding the "hole coordinate" x_κ if it otherwise would be included in this set),

$$\tilde{A}_{i_1 \cdots i_f}^{(\kappa)} = \sum_{j_1=1}^{n_1} \cdots \sum_{j_{\kappa-1}=1}^{n_{\kappa-1}} \sum_{j_{\kappa+1}=1}^{n_{\kappa+1}} \cdots \sum_{j_{z_n}=1}^{n_{z_n}} \langle q_i^{(1)} | \phi_{j_1}^{(1)} \rangle \cdots \langle q_i^{(\kappa-1)} | \phi_{j_{\kappa-1}}^{(\kappa-1)} \rangle \langle q_i^{(\kappa+1)} | \phi_{j_{\kappa+1}}^{(\kappa+1)} \rangle \cdots \langle q_i^{(z_n)} | \phi_{j_{z_n}}^{(z_n)} \rangle A_{j_1 \cdots j_{\kappa-1} i_\kappa j_{\kappa+1} \cdots j_{z_n} i_{z_n+1} \cdots i_f}.$$

If the "hole coordinate" x_κ is in the set of "grid coordinates" $x_1, x_2, \ldots, x_{z_n}$, the contributions to the single-hole matrices are given as

$$\langle \hat{H}_n \rangle_{kl}^{(\kappa)} = \sum_{j_{z_n+1}=1}^{n_{z_n+1}} \cdots \sum_{j_f=1}^{n_f} \sum_{i_1=1}^{n_1} \cdots \sum_{i_{\kappa-1}=1}^{n_{\kappa-1}} \sum_{i_{\kappa+1}=1}^{i_{\kappa+1}} \cdots \sum_{i_f=1}^{n_f} \tilde{A}_{i_1 \cdots i_{\kappa-1} k i_{\kappa+1} \cdots i_f}^{(\kappa)*} \tilde{A}_{i_1 \cdots i_{\kappa-1} l i_{\kappa+1} \cdots i_{z_n} j_{z_n+1} \cdots j_f}^{(\kappa)} V(q_{i_1}^{(1)}, \ldots, q_{i_{\kappa-1}}^{(\kappa-1)}, x_\kappa, q_{i_{\kappa+1}}^{(\kappa+1)}, \ldots, q_{i_{z_n}}^{(z_n)})$$
$$\times \langle \phi_{i_{z_n+1}}^{(z_n+1)} | \hat{h}_n^{(z_n+1)} | \phi_{j_{z_n+1}}^{(z_n+1)} \rangle \cdots \langle \phi_{i_f}^{(f)} | \hat{h}_n^{(f)} | \phi_{j_f}^{(f)} \rangle. \tag{D11}$$

If the hole coordinate x_κ is in the set of "basis coordinates" $x_{z_n+1}, \ldots, x_f$, the contributions to the single-hole matrices read

$$\langle \hat{H}_n \rangle_{kl}^{(\kappa)} = \sum_{i_1=1}^{n_1} \cdots \sum_{i_{\kappa-1}=1}^{n_{\kappa-1}} \sum_{i_{\kappa+1}=1}^{i_{\kappa+1}} \cdots \sum_{i_f=1}^{n_f} \tilde{A}_{i_1 \cdots i_{\kappa-1} k i_{\kappa+1} \cdots i_f}^{(\kappa)*} \sum_{j_1=1}^{n_1} \cdots \sum_{j_{\kappa-1}=1}^{n_{\kappa-1}} \sum_{j_{\kappa+1}=1}^{j_{\kappa+1}} \cdots \sum_{j_f=1}^{n_f} \tilde{A}_{j_1 \cdots j_{\kappa-1} l j_{\kappa+1} \cdots j_f}^{(\kappa)}$$
$$\times \langle q_{i_1}^{(1)} \cdots q_{i_{z_n}}^{(z_n)} | V_n(x_1, \ldots, x_{z_n}) | q_{j_1}^{(1)} \cdots q_{j_{z_n}}^{(z_n)} \rangle \langle \phi_{i_{z_n+1}}^{(z_n+1)} | \hat{h}_n^{(z_n+1)} | \phi_{j_{z_n+1}}^{(z_n+1)} \rangle \cdots \langle \phi_{i_{\kappa-1}}^{(\kappa-1)} | \hat{h}_n^{(\kappa-1)} | \phi_{j_{\kappa-1}}^{(\kappa-1)} \rangle \hat{h}_n^{(\kappa)}$$
$$\times \langle \phi_{i_{\kappa+1}}^{(\kappa+1)} | \hat{h}_n^{(\kappa+1)} | \phi_{j_{\kappa+1}}^{(\kappa+1)} \rangle \cdots \langle \phi_{i_f}^{(f)} | \hat{h}_n^{(f)} | \phi_{j_f}^{(f)} \rangle. \tag{D12}$$

[1] D. W. Turner, C. Baker, and C. R. Brundle, *Molecular Photoelectron Spectroscopy* (Wiley, London, 1970).
[2] A. W. Potts and W. C. Price, Proc. R. Soc. London, Ser. A **326**, 181 (1972).
[3] M. S. Banna and D. A. Shirley, J. Chem. Phys. **63**, 4759 (1975).
[4] M. N. Piancastelli, C. Cauletti, and M. Y. Adam, J. Chem. Phys. **87**, 1982 (1987).
[5] D. Edvardsson, P. Baltzer, L. Karlsson, B. Wannberg, D. M. P. Holland, D. A. Shaw, and E. E. Rennie, J. Phys. B **32**, 2583 (1999).
[6] H. Ågren, I. Reineck, H. Veenhuizen, R. Maripuu, R. Arneberg, and L. Karlson, Mol. Phys. **45**, 477 (1982).
[7] P. Botschwina, in *Ion and Cluster Ion Spectroscopy and Structure*, edited by J. P. Maier (Elsevier, Amsterdam, 1989).
[8] E. Haller, L. S. Cederbaum, W. Domcke, and H. Köppel, Chem. Phys. Lett. **72**, 427 (1980).
[9] G. Dujardin and S. Leach, Can. J. Chem. **63**, 1386 (1985).
[10] C. Krier, M. T. Praet, and J. C. Lorquet, J. Chem. Phys. **82**, 4073 (1985).
[11] C. Woywod, S. Scharfe, R. P. Krawczyk, and W. Domcke, J. Chem. Phys. **118**, 5880 (2003).
[12] M. H. Perrin and M. Gouterman, J. Chem. Phys. **46**, 1019 (1967).
[13] J. H. van der Waals, A. M. D. Berghuis, and M. S. de Groot, Mol. Phys. **13**, 301 (1967).
[14] M. Z. Zgierski and M. Pawlikowski, J. Chem. Phys. **70**, 3444 (1979).
[15] H. Köppel, W. Domcke, and L. S. Cederbaum, Adv. Chem. Phys. **57**, 59 (1984).
[16] W. Lichten, Phys. Rev. **131**, 229 (1963).
[17] F. T. Smith, Phys. Rev. **179**, 111 (1969).
[18] M. Baer, Chem. Phys. Lett. **35**, 112 (1975).
[19] H. C. Longuet-Higgins, Adv. Spectrosc. (N.Y.) **2**, 429 (1961).
[20] I. B. Bersuker and V. Z. Polinger, *Vibronic Interactions in Molecules and Crystals* (Springer, Berlin, 1989).
[21] G. Herzberg and H. C. Longuet-Higgins, Discuss. Faraday Soc. **35**, 77 (1963).
[22] W. Domcke, D. R. Yarkony, and H. Köppel, *Conical Intersections: Electronic Structure, Dynamics and Spectroscopy* (World Scientific, Singapore, 2003).
[23] C. Léonard, S. Carter, N. C. Handy, and P. J. Knowles, Mol. Phys. **99**, 1335 (2001).
[24] C. Léonard, S. Carter, and N. C. Handy, Phys. Chem. Chem. Phys. **4**, 4087 (2002).
[25] C. Léonard, N. C. Handy, S. Carter, and J. M. Bowman, Spectrochim. Acta, Part A **58**, 825 (2002).
[26] T. Rajamäki, A. Miani, J. Pesonen, and L. Halonen, Chem. Phys. Lett. **363**, 226 (2002).
[27] T. Rajamäki, A. Milani, and L. Halonen, J. Chem. Phys. **118**, 10929 (2003).
[28] H. Lin, W. Thiel, S. N. Yurchenko, M. Carvajal, and P. Jensen, J. Chem. Phys. **117**, 11265 (2002).
[29] W. Domcke and G. Stock, Adv. Chem. Phys. **100**, 1 (1997).
[30] A. Viel and W. Eisfeld, J. Chem. Phys. **120**, 4603 (2004).

[31] W. Eisfeld and A. Viel, J. Chem. Phys. **122**, 204317 (2005).
[32] C. Woywod, W. Domcke, A. L. Sobolewski, and H.-J. Werner, J. Chem. Phys. **100**, 1400 (1994).
[33] T. H. Dunning, Jr., J. Chem. Phys. **90**, 1007 (1989).
[34] R. A. Kendall, T. H. Dunning, Jr., and R. J. Harrison, J. Chem. Phys. **96**, 6769 (1992).
[35] H.-J. Werner, P. J. Knowles, R. D. Amos *et al.*, MOLPRO is a package of *ab initio* programs.
[36] These factors are arbitrary. They result from the choice of combined distortions in symmetry coordinates, which were not normalized when performing the *ab initio* calculations and are thus a result of the normalization performed afterwards.
[37] H. D. Meyer, U. Manthe, and L. S. Cederbaum, Chem. Phys. Lett. **165**, 73 (1990).
[38] U. Manthe, H. D. Meyer, and L. S. Cederbaum, J. Chem. Phys. **97**, 3199 (1992).
[39] M. H. Beck and H. D. Meyer, Z. Phys. D: At., Mol. Clusters **42**, 113 (1997).
[40] U. Manthe, J. Chem. Phys. **105**, 6989 (1996).
[41] R. van Harrevelt and U. Manthe, J. Chem. Phys. **123**, 064106 (2005).